Prediction of the Equilibrium Structures and Photomagnetic Properties of the Prussian Blue Analogue RbMn[Fe(CN)$_6$] by Density Functional Theory

Javier Luzon,[†] Miguel Castro,[‡] Esther J. M. Vertelman,[†,§] Régis Y. N. Gengler,[†] Petra J. van Koningsbruggen,[†,§] Olga Molodtsova,[||] Martin Knupfer,[||] Petra Rudolf,[†] Paul H. M. van Loosdrecht,[†] and Ria Broer*,[†]

Zernike Institute for Advanced Materials and Stratingh Institute for Chemistry, University of Groningen, Nijenborgh 4, 9747 AG Groningen, The Netherlands, Instituto de Ciencia de Materiales de Aragón, CSIC−Universidad de Zaragoza, 50009 Zaragoza, Spain, and IFW Dresden, P.O. Box 270116, D-01171 Dresden, Germany

Received: January 9, 2008; Revised Manuscript Received: April 9, 2008

A periodic density functional theory method using the B3LYP hybrid exchange-correlation potential is applied to the Prussian blue analogue RbMn[Fe(CN)$_6$] to evaluate the suitability of the method for studying, and predicting, the photomagnetic behavior of Prussian blue analogues and related materials. The method allows correct description of the equilibrium structures of the different electronic configurations with regard to the cell parameters and bond distances. In agreement with the experimental data, the calculations have shown that the low-temperature phase (LT; Fe^{2+}(t$^6_{2g}$, $S = 0$)−CN−Mn^{3+}(t$^3_{2g}$e^1_g, $S = 2$)) is the stable phase at low temperature instead of the high-temperature phase (HT; Fe^{3+}(t$^5_{2g}$, $S = 1/2$)−CN−Mn^{2+}(t$^3_{2g}$e^2_g, $S = 5/2$)). Additionally, the method gives an estimation for the enthalpy difference (HT ⇔ LT) with a value of 143 J mol^{-1} K^{-1}. The comparison of our calculations with experimental data from the literature and from our calorimetric and X-ray photoelectron spectroscopy measurements on the Rb$_{0.97}$Mn[Fe(CN)$_6$]$_{0.98}$·1.03H$_2$O compound is analyzed, and in general, a satisfactory agreement is obtained. The method also predicts the metastable nature of the electronic configuration of the high-temperature phase, a necessary condition to photoinduce that phase at low temperatures. It gives a photoactivation energy of 2.36 eV, which is in agreement with photoinduced demagnetization produced by a green laser.

Introduction

Recently, the development of photomagnetic molecular materials, in which magnetic properties can be controlled by light, has drawn increasing interest due to their potential relevance for high-density data storage and other technological applications (for a review see ref 1 and references therein). Several types of molecular materials with photomagnetic properties have been synthesized in the past few years. Some representative examples are (i) Fe^{2+} and Fe^{3+} spin crossover compounds, in which a switching between spin states is photoinduced[2–8] (LIESST = light-induced excited spin state trapping) or triggered by a photoisomerization of a ligand[9–13] (LD-LISC = ligand-driven light-induced spin change), and (ii) valence tautomeric compounds such as Co^{2+}−semiquinone[14–16] or Mn^{2+}−semiquinone[17–20] complexes.

In this research field, one of the most promising families are Prussian blue analogues (PBAs) because they exhibit the novel phenomenon of optically controllable spontaneous magnetic ordering.[21–24] In these molecular compounds, with the general formula A$_x$M[M′(CN)$_6$]$_{(2+x)/3}$·zH$_2$O, the first-row transition metals M and M′ are bridged by cyanide groups, forming a 3-D network structure usually containing interstitial ions (A) and water molecules. In addition, these compounds commonly have vacancies of the hexacyanometalate unit M′(CN)$_6$.

In K$_{0.2}$Co$_{1.4}$[Fe(CN)$_6$]·6.9H$_2$O, the first reported photomagnetic PBA,[21,22] light irradiation at low temperatures produces a permanent increase of the magnetization, an effect that can be reversed by blue light irradiation. From the same family, two other photomagnetic behaviors have been observed to date: a photoinduced demagnetization in RbMn[Fe(CN)$_6$][23] and a photoinduced magnetic pole inversion[24] in (Fe$_{0.40}$Mn)[Cr(CN)$_6$]·7.5H$_2$O. Furthermore, some related materials such as nitroprussides[25–28] and 4d-transition-metal cyanides[29–32] have also shown photomagnetism.

The generation of photomagnetic behavior within such materials appears to require particular, often rather subtle, compositional and structural features, the details of which are basically unknown at this stage. This will have to be evaluated if one attempts the rational design of this type of switchable magnetic material. Evidently, the targeted exploitation of the vast synthetic flexibility of the PBAs and other related compounds necessitates the development of a theoretical method that is able to predict which of these materials could be candidates for showing photomagnetic behavior.

In this work we tested the suitability of periodic density functional theory (DFT) with the hybrid B3LYP[33] exchange-correlation functional for describing the physics underlying the photoinduced magnetic behavior in the PBAs. The B3LYP functional, which mixes 20% Fock exchange with a "pure" nonlocal exchange correlation functional, has been shown to be able to yield much better orbital band gaps than pure functionals in several transition-metal compounds. See, for example, refs 34 and 35.

* To whom correspondence should be addressed. Phone: +31 050 363 4374. Fax: +31 50 363 4441. E-mail: R.Broer@rug.nl.
† Zernike Institute for Advanced Materials, University of Groningen.
‡ CSIC−Universidad de Zaragoza.
§ Stratingh Institute for Chemistry, University of Groningen.
|| IFW Dresden.

For our study we chose the RbMn[Fe(CN)$_6$] compound since the photomagnetism is observed in this compound with a well-defined stoichiometry devoid of hexacyanometalate vacancies that would complicate the calculations and the analysis of the results.

RbMn[Fe(CN)$_6$] exhibits a phase transition from a high-temperature cubic structure ($F\bar{4}3m$) (HT phase) to a low-temperature tetragonal one ($I\bar{4}m2$) (LT phase) around 250 K.[36,37] This structural transition is related to an entropy-driven charge transfer from the Mn ion to the Fe ion,[38] which is described as Fe^{3+}(t$^5_{2g}$, S = 1/2)−CN−Mn^{2+}(t$^3_{2g}$e^2_g, S = 5/2) → Fe^{2+}(t$^6_{2g}$, S = 0)−CN−Mn^{3+}(t$^3_{2g}$e^1_g, S = 2). The tetragonal nature of the LT phase is due to the Jahn−Teller distortion of the Mn^{3+} ion because the depopulation of the d$_{x^2−y^2}$ orbital produces a shortening of the Mn−N distances in the four N atoms headed by that e$_g$ orbital.

The photomagnetic behavior of this compound[23] has been explained by considering that the illumination with a green laser (532 nm) of the LT phase produces a charge transfer from iron to manganese, resulting in a Franck−Condon state, i.e., a vertical electronic excitation from the LT electronic configuration to the HT electronic configuration, without a change of the nuclear structure. Beyond a laser intensity threshold, the microstructural relaxations of the photoexcited electronic configurations produce a structural transition to a photoinduced metastable phase with a paramagnetic behavior instead of the ferromagnetic behavior of the LT phase below 12 K.[39] This different magnetic behavior of the LT and HT phases explains the observed photoinduced demagnetization at low temperatures produced by green laser illumination.

In the next sections, after introducing the theoretical methodology, the calorimetric and X-ray photoelectron spectroscopy (XPS) experiments used to support the theoretical issues, we will present the results of the DFT calculations on the RbMn-[Fe(CN)$_6$] compound. In particular, we have computed the equilibrium structures together with their energies for the two different electronic configurations. The results are analyzed in relation to the thermally induced phase transition. We also computed the potential energy surface (PES) of the two electronic configurations and the photoactivation energy to produce an electron transfer from the ground to the metastable electronic configuration at low temperature. The results of these last computations are directly related to the photomagnetic behavior shown by the RbMn[Fe(CN)$_6$] compound.

Experimental and Computational Details

Experimental Details. To test the correctness of some of our computational results, we performed a calorimetric measurement by differential scanning calorimetry (DSC) on sample **3** of ref 40 (Rb$_{0.97}$Mn[Fe(CN)$_6$]$_{0.98}$·1.03H$_2$O). In the previous reference the synthesis of the compound is reported in detail.

DSC measurements were performed in the 100−330 K temperature range at a scan rate of 10 °C/min, using a differential scanning calorimeter, Q1000, from TA Instruments. The measurements were carried out using 4.81 mg of powdered sample sealed in aluminum pans with a mechanical crimp. Temperature and enthalpy calibrations were made with standard samples of indium, using its melting transition (429.76 K, 3.296 kJ mol^{-1}), and with a sample of Mn$_3$GaC, using its ferro- to antiferromagnetic transition (171.83 K, 713 J mol^{-1}). Overall accuracies of ±0.5 K in temperature and ±5% in the enthalpy contents are estimated. The uncertainty for the determination

of the anomalous enthalpy and entropy increases due to the difficulty in tracing the baselines (especially for the cooling mode).

XPS data were collected at the IFW Leibniz Institute for Solid State and Materials Research in Dresden, using a SPECS PHOIBOS-150 spectrometer with a base pressure of 1 × 10^{-10} Torr, equipped with a monochromatic Al Kα X-ray source ($h\nu$ = 1486 eV). The photoelectron takeoff angle was 90°, and an electron flood gun was used to compensate for sample charging. An evaporated gold film supported on mica served as the substrate. Compound Rb$_{0.97}$Mn[Fe(CN)$_6$]$_{0.98}$·1.03H$_2$O in powdered form was dispersed in distilled−deionized (18.2 MΩ cm at 25 °C) water, the dispersion was stirred for 5 min, and a few drops of the suspension was left to dry in air on the substrate. The sample was introduced into an ultrahigh vacuum as soon as dry and placed on a He-cooled cryostat equipped with a Lakeshore Cryogenic temperature controller to explore the 50−350 K temperature range. All binding energies were referenced to the nitrogen signal at 398 eV (cyanide groups). No X-ray-induced sample degradation was detected. Spectral analysis included a Tougaard background subtraction[41] and peak deconvolution employing Gaussian line shapes using the Win-Spec program developed at LISE Laboratory, University of Namur, Belgium.

Computational Details. All calculations were performed using the periodic code CRYSTAL03[42] within the framework of the DFT. The exchange-correlation contribution to the total electronic energy was accounted for by the hybrid functional B3LYP.[33] This hybrid DFT approach has proved to provide an overall balanced description of most of the relevant properties of transition-metal compounds, improving, in general, the accuracy of pure DFT methods such as LDA or GGA (for instance, see ref 43 and references therein). In the case of the Rb atoms a small-core Hay−Wadt pseudopotential to represent the core−electrons was used in combination with an ionic valence basis set.[44] The other atomic centers were described by all-electron basis sets: 86-411(d41)G for Fe and Mn and 6-21G* for C and N.[44] The reciprocal space was sampled according to a regular sublattice with a shrinking factor of 8, corresponding to 59 independent k points in the irreducible Brillouin zone.

For the geometry optimizations of the atomic positions with fixed cell parameters the thresholds for the maximum and the root-mean-square (rms) forces were set to 0.00045 and 0.00030 au, respectively, and the thresholds for the maximum and the rms atomic displacements were set to 0.00180 and 0.00120 au, respectively. The optimization was considered complete when the four conditions were satisfied simultaneously.

All calculations were carried out by considering the symmetry of the tetragonal space group of the LT phase, $I\bar{4}m2$, since it is the space group with the lowest symmetry and it is a subgroup of the cubic space group of the HT phase, $F\bar{4}3m$.

Computation of the HT and LT electronic configurations was done by forcing the total spin quantum number of the primitive unit cell to be S = 3 and S = 2, respectively. It is worth noting that, in all the cases, when the spin quantum number was forced, the system converged to the aimed electronic configuration. This indicates that for that nuclear structure and that spin value the aimed electronic configuration was indeed the lowest energy state, thus justifying the application of the DFT method.

Results and Discussion

Equilibrium Structures. The cell parameters of the LT and HT equilibrium structures were obtained by computing their

TABLE 1: Free Energies and Cell Parameters of the Computed Equilibrium Structures[a]

phase	energy (au)	a, b (Å)	c (Å)
HT	-2995.0277	$7.51 = 10.62/\sqrt{2}$	10.60 (10.56)
LT	-2995.0419	7.14 (7.09)	10.64 (10.53)

[a] Cell parameters in parentheses are the experimental values from ref 45.

relative energy gradients after optimizing the atomic positions for each set of cell parameters. The total energies per unit cell and the cell parameters for the two equilibrium structures are presented in Table 1. The computed cell parameters of the two equilibrium structures are close to the experimental values.[45] In particular, in the case of the HT electronic configuration, the equilibrium structure has almost converged to the cubic structure as observed experimentally.

The equilibrium structure of the LT electronic configuration has a free energy lower than the free energy corresponding to the equilibrium structure of the HT electronic configuration. This result is in agreement with experiments which show that the LT phase is thermodynamically more stable than the HT phase in the low-temperature region. Since the $Rb_{0.97}Mn[Fe(CN)_6]_{0.98} \cdot 1.03H_2O$ compound undergoes a thermally induced phase transition between the two electronic configurations at $T_{1/2}^{av} = 269$ K ($T_{1/2}^{\downarrow} = 240$ K to $T_{1/2}^{\uparrow} = 297$ K)[40] ($T_{1/2}$ is the characteristic temperature at which there is 50% of the low-temperature phase and 50% of the high-temperature phase; this temperature is evaluated on heating and cooling, and $T_{1/2}^{av}$ is its average value), the computed free energy difference of 0.386 eV (37.2 kJ mol^{-1}) implies an entropy difference of 138 J K^{-1} mol^{-1} between the LT and HT phases. In the literature two calorimetric studies report very different values for the differences in free energy and entropy. In one of them,[46] the reported values are $\Delta H = 11-14$ kJ mol^{-1} and $\Delta S = 48-59$ J K^{-1} mol^{-1}, i.e., values that are of the same order of magnitude as our computational results and experimental data (see below). However, in the earliest calorimetric study[47] the values were only 1.7 kJ mol^{-1} and 6 J K^{-1} mol^{-1}, respectively, for the free energy and entropy differences, i.e., 1 order of magnitude smaller than our results. Although in that work[47] the measurements were performed on the stoichiometric $RbMn[Fe(CN)_6]$ compound without water molecules and therefore without vacancies, the results are rather puzzling since the value of ΔS from the latter calorimetric study is even lower than the theoretical spin contribution to the difference in the entropy, 16.4 J K^{-1} mol^{-1}. Moreover, the contraction of the Fe$-$Mn distances in the ab plane of around 0.25 Å from the HT phase to the LT phase should result in an important vibrational contribution to the entropy variation.

To test the validity of our computational results, we carried out calorimetric measurements on the compound $Rb_{0.97}Mn[Fe(CN)_6]_{0.98} \cdot 1.03H_2O$.[40] These measurements were performed in the temperature range of $100-330$ K for both heating and cooling processes. The heat capacity anomalies corresponding to the HT ⇌ LT transitions after subtraction of the baselines are shown in Figure 1. The critical temperatures, defined as the maxima of the peaks, are 244 and 298 K for the cooling and heating modes, respectively. These values are in good agreement with the characteristic transition temperatures, $T_{1/2}^{\downarrow} = 240$ K to $T_{1/2}^{\uparrow} = 297$ K, obtained from the magnetic measurements.[40] The experimentally determined enthalpy and entropy variations associated with the LT ⇌ HT phase transition are $\Delta H = 18 \pm 1$ kJ mol^{-1} and $\Delta S = 60 \pm 5$ J K^{-1} mol^{-1} for the heating mode and $\Delta H = 19 \pm 1$ kJ mol^{-1} and $\Delta S = 80 \pm 5$ J K^{-1} mol^{-1} for
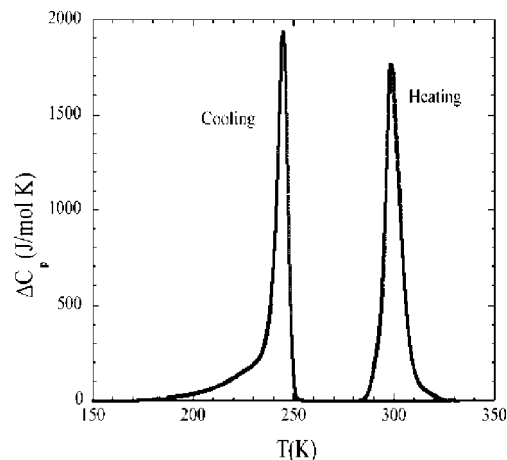

Figure 1. Heat capacity anomalies (on heating and cooling) corresponding to the thermally induced transition for the $Rb_{0.97}Mn[Fe(CN)_6]_{0.98} \cdot 1.03H_2O$ compound.

the cooling mode. The higher values for the cooling mode are related to the difficulty in tracing the baseline, which must contribute the tail observed in the heat capacity anomaly at low temperature.

Although the experimental values from ref 46 are of the same order as our results, they are still lower than our calculated and measured values. However, the studied samples in ref 46 were $Rb_{0.58}Mn[Fe(CN)_6]_{0.82} \cdot 4.04H_2O$ and $Rb_{0.85}Mn[Fe(CN)_6]_{0.96} \cdot 1.40H_2O$, i.e., compounds with vacancies at the Rb and at the Fe sites. The existence of vacancies in $Rb_{1-x}Mn[Fe(CN)_6]_{1-y} \cdot zH_2O$ produces an incomplete conversion between the LT and HT electronic configurations in the thermal phase transition;[40] hence, the determined variation in thermodynamic parameters will necessarily be smaller than the actual molar enthalpy and entropy changes for a complete phase transition.

Our experimental enthalpy and entropy variations are between half and two-thirds of the values from the periodic DFT calculations. This same order of qualitative agreement between B3LYP periodic DFT calculations and experimental data has also been obtained in a study of the transition enthalpies for a range of SiO_2 phases.[48] Although the agreement is not quantitatively as good as we might wish, the computational method is able to give the order of magnitude of the enthalpy difference between two phases with different electronic configurations. As we will explain more in detail later, this, combined with the observation that we are able to correctly describe the geometry of the LT and HT phases, opens the possibility to apply this computational method to the prediction of possible candidates for showing photomagnetic properties. This will mean an important reduction in the synthetic work needed.

Moreover, although the compound used in the calorimetry experiment, $Rb_{0.97}Mn[Fe(CN)_6]_{0.98} \cdot 1.03H_2O$, is almost stoichiometric, several physical characterization experiments indicate an incomplete HT ⇌ LT phase conversion, which can partially account for the difference between the calorimetric and computational values. First, X-ray powder diffraction[40] indicated that the compound $Rb_{0.97}Mn[Fe(CN)_6]_{0.98} \cdot 1.03H_2O$ presents at room temperature 91.1% HT and 8.9% LT phases. Second, a ^{57}Fe Mössbauer spectrum[40] did not show at 80 K the existence of the HT phase, yet its presence cannot be excluded. For this type of material it turns out that the Mössbauer lines of LS Fe^{2+} and LS Fe^{3+} do overlap, which does not allow the accurate estimation of their relative contribution in cases where either one is present in a small amount. In addition, in this work we have performed an XPS experiment as a direct method for
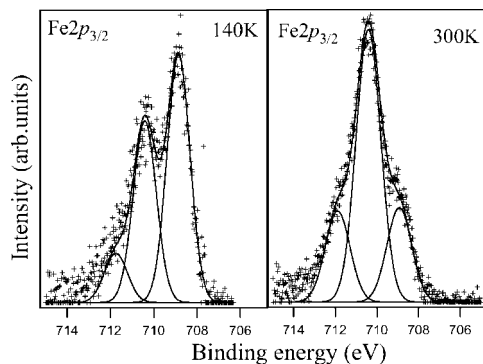
Figure 2. Fe 2p$_{3/2}$ core level photoemission spectra of Rb$_{0.97}$Mn[Fe-(CN)$_6$]$_{0.98}$·1.03H$_2$O collected at room temperature and 140 K. The fits to the raw data are also plotted.

TABLE 2: Transition-Metal–Ligand Distances of the LT and HT Equilibrium Structures Computed by Periodic DFT and from Published Experimental Works[a]

phase	source	Mn–N$_{xy}$	Mn–N$_z$	Fe–C$_{xy}$	Fe–C$_z$
LT	calculation	1.97	2.20	1.91	1.94
LT	ref 39	1.96	2.20	1.92	1.89
LT	ref 45	1.99	2.27	1.89	1.83
LT	ref 49	1.96	2.21	1.90	1.90
LT	ref 50	1.91	2.28	1.98	1.86
HT	calculation	2.18	2.19	1.94	1.94
HT	ref 51	2.20	2.20	1.92	1.92
HT	ref 45	2.18	2.18	1.92	1.92
HT	ref 49	2.19	2.19	1.93	1.93
HT	ref 50	1.82	1.94	2.23	2.30

[a] *xy* denotes the *ab* plane, and *z* denotes the *c* axis. Units are angstroms.

identifying the oxidation states of Mn and Fe at the compound surface. Figure 2 shows the Fe 2p$_{3/2}$ core level photoemission spectrum of compound Rb$_{0.97}$Mn[Fe(CN)$_6$]$_{0.98}$·1.03H$_2$O at room temperature and at 140 K, as well as fits to the raw data.

At both temperatures, the Fe 2p$_{3/2}$ signal consists of three distinct contributions: the Fe^{2+} line at 708.8 eV binding energy, the Fe^{3+} line at 710.5 eV, and the Fe^{3+} satellite at 711.7 eV. Comparing the relative intensities of the Fe^{2+} and Fe^{3+} components in the room temperature spectrum suggests a near-surface composition of 76% Fe^{3+} and 24% Fe^{2+}. After slow cooling ($\sim$2 K/min) of the sample to 252 K, a temperature just above the HT to LT phase transition, no spectral changes are detected with respect to the room temperature data (not shown). Further cooling to 140 K induces a change of the Fe 2p$_{3/2}$ photoemission spectrum: at 140 K the near-surface ratio is 48% Fe^{3+} and 52% Fe^{2+}. Although it must be taken into account that XPS is a surface technique and that the structure and composition of the surface can largely differ from the structure and composition in the bulk material, these results clearly support the interpretation that the conversion HT $\Leftrightarrow$ LT is incomplete.

Although the computational method is able to describe qualitatively the relative energy between both electronic configurations, there are other tests that must be overcome to confirm the validity of this theoretical method for describing the physics of the photomagnetic PBAs. One of them is a correct prediction of the interatomic distances for the equilibrium structures of the ground and the charge transfer phases. Table 2 shows the Mn–N and Fe–C interatomic distances for the optimized equilibrium structures of both LT and HT phases and the experimental values that have been published in other papers.[39,45,49–51] The theoretical values are in agreement with

TABLE 3: Computed Charges and Spin Populations of the LT and HT Equilibrium Structures[a]

		Fe	Mn	Nxy	Nz	Cxy	Cz	Rb
LT	charge	0.90	1.80	−0.78	−0.74	0.18	0.09	1.00
LT	spin	0.09	3.75	0.05	0.02	−0.05	0.06	0.00
HT	charge	1.14	1.64	−0.71	−0.73	0.09	0.08	1.00
HT	spin	1.06	4.74	0.06	0.01	−0.02	0.01	0.00

[a] *xy* denotes the *ab* plane, and *z* denotes the *c* axis. Units are electrons (charge) and Bohr magnetons (spin).

neutron,[39,51] EXAFS,[49] and X-ray[45] diffraction data, but some important differences exist with respect to another X-ray experiment.[50] In particular, in this work the authors obtain values for the Mn–N and Fe–C distances in the HT phase that are qualitatively similar to the Fe–C and Mn–N distances, respectively, found in our calculations and in the other experimental works. It seems that they have interchanged Fe with Mn and C with N in the analysis of their X-ray data, maybe due to their similar electronic charges, which also can explain why the Fe–C and Mn–N distances in both HT and LT phases do not quantitatively agree with those of the other works. Similar Fe–C and Mn–N distances from another X-ray experiment[37] were proposed to proceed from a wrong local minimum in an addendum to ref 37. Therefore, without considering this X-ray experiment, our theoretical method predicts correctly the interatomic distances in the RbMn[Fe(CN)$_6$] compound.

To complete the section devoted to the calculation of the equilibrium structures, we have listed in Table 3 the charge and spin atomic populations according to a Mulliken population analysis for all the atoms for the LT and HT equilibrium structures obtained from the periodic DFT calculations. The spin populations are in agreement with the spin states of the iron and manganese ions in both LT and HT electronic configurations, confirming a correct convergence of the calculations to those electronic configurations.

Energy Surfaces. Being able to compute the equilibrium structures and their free energies for the different electronic configurations of a PBA, as done in the previous section for RbMn[Fe(CN)]$_6$, allows the study of the thermally induced phase transition between two electronic configurations with close enthalpies and with different entropies (if the phase with a lower enthalpy also has a lower entropy). Moreover, knowing the enthalpy difference between both equilibrium structures also gives a hint about the possibility of a photoinduced electron transfer from the ground electronic configuration to the other electronic configuration. However, this possibility is not the only condition for a photoinduced phase transition. A second condition is that the equilibrium structure corresponding to the photoinduced electronic configuration must be metastable; i.e., an energy potential barrier must be overcome to return to the equilibrium structure of the ground electronic configuration.

To investigate the existence of a potential energy barrier is not enough to compute the equilibrium structure energies for the different electronic configurations. Instead a potential energy surface of the different electronic configurations as a function of the structural parameters must be performed. Figure 3 represents a PES of both the HT and LT electronic configurations. The represented PES is a function of the *a* and *b* cell parameters, with the *c* cell parameter fixed to an average experimental value of 10.54 Å. Since the *c* parameters in the two phases differ by only 0.03 Å, this is not a severe restriction. A similar PES surface is obtained using a fixed *c* cell parameter from the computed equilibrium structures instead of the average experimental value. Since the experiment and the computed
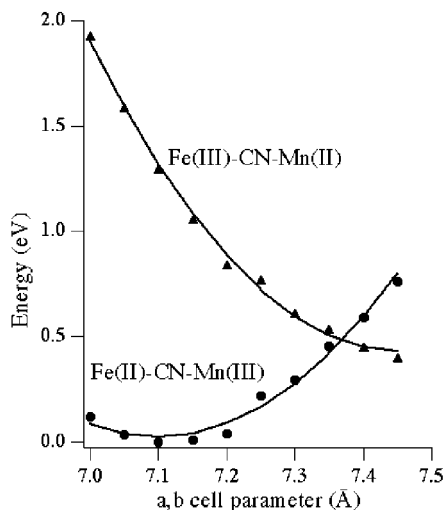
5746 *J. Phys. Chem. A, Vol. 112, No. 25, 2008*

Luzon et al.

Figure 3. Potential energy surfaces for both LT and HT phases as function of the $a = b$ cell parameters.

TABLE 4: Madelung Potential at the Mn and Fe Positions Created by Both HT and LT Electronic Configurations for Models 1 and 2[a]

model	Mn(LT)	Mn(HT)	Fe(LT)	Fe(HT)
1	−6.49	−4.29	12.99	10.79
2	−3.56	−3.18	9.65	9.28

[a] See the text. Units are electronvolts.

equilibrium structures indicate that the HT phase is cubic ($a = b = c/\sqrt{2}$) and the LT phase is tetragonal with $a = b < c/\sqrt{2}$, the PES is restricted to the region $a = b \leq c/\sqrt{2}$ (1.45 Å). In each point of the PES the atomic coordinates were optimized independently for both electronic configurations.

As already obtained in the calculation of the HT and LT equilibrium structures, the PES surface yields the LT electronic configuration as the ground state. In addition, the equilibrium structure of the HT electronic configuration is indeed a local energy minimum. The correct description of the metastable nature of the HT phase is an important result to consider this method suitable for the prediction of photomagnetism in PBAs and related materials.

Photoactivation Energy. As a final point the periodic DFT method was also used for the computation of the photoactivation energy. Since the absorption of one photon is supposed to produce a vertical excitation from the LT electronic configuration to the HT electronic configuration, we calculated the difference in energy between the LT and HT electronic configurations using the optimized crystal structure for the LT electronic configuration. This photoactivation energy is 2.36 eV, corresponding to a photon of wavelength 525 nm, a value close to the experimental value of around 532 nm.[23]

Although in this case the calculation of the photoactivation energy agrees with the experimental value, before stating that this computational method is suitable for estimating the photoactivation energy, we must clarify two points.

First, for future application of this method in other PBAs, it is important to remark that the calculation of the photoactivation energy would not have been formally possible if the HT electronic configuration were the ground state and the LT electronic configuration the excited state. The reason is that in that case the ground state for the total spin $S = 2$ would have been the antiferromagnetic arrangement of the HT electronic configuration ($S = 5/2$ (Mn^{2+}) − 1/2 (Fe^{3+})). Therefore, the LT electronic configuration, not being the ground state for $S = 2$, could not be computed using a DFT method (let us remember that the computations are performed using the optimized crystal structure of the ground state, i.e., the HT electronic configuration in that case).

Second, in the real physical system the photoactivation charge transfer is a local phenomenon where an electron is transferred from one Fe^{2+} ion to a neighboring Mn^{3+} ion. This $Fe^{2+}-Mn^{3+}$

pair is embedded in a crystal with a ratio of $Fe^{2+}-Mn^{3+}$ to $Fe^{3+}-Mn^{2+}$ pairs depending on the progress of the photoactivated phase transition. However, in the periodic calculation, the electronic configurations for the initial and the final states are $Fe^{2+}-Mn^{3+}$ and $Fe^{3+}-Mn^{2+}$, respectively, in the entire crystal. The main problem of the inability of the periodic method to correctly compute the photoactivation energy lies in the incorrect description of the rest of the crystal that is not involved in the photoactivation charge transfer process. In particular, it is mostly due to the incorrect electrostatic potential created by the rest of the crystal, the Madelung potential, in the space region involved in the charge transfer. Since the charge distributions of the initial ground state and the final Franck−Condon state are different, the photoactivation energy depends on the shape of the Madelung potential (created by the rest of the crystal) in the space region where there is a difference in the electron density between both states.

Let us denote the Madelung potentials created by the rest of the crystal with the electronic charge distribution for the Fe and Mn ions of the real system as $V_M(r)$ and for the LT and HT periodic systems as $V_M^{LT}(r)$ and $V_M^{HT}(r)$, respectively. Using the crude approximation $V_M(r) = (V_M^{LT}(r) + V_M^{HT}(r))/2$, we can write the following expression for the overestimation of the Madelung potential effect (ΔE_M) in the calculation of the photoactivation energy with the periodic DFT method:

$$\Delta E_M \approx \frac{1}{2} \int \left(V_M^{LT}(r) - V_M^{HT}(r) \right) \Delta\rho(r) \, \partial v \quad (1)$$

where $\Delta\rho(r)$ is the charge density difference between the LT ground and the Franck−Condon states. To estimate this ΔE_M value, we calculated the V_M^{LT} and V_M^{HT} Madelung potentials created by the rest of the crystal inside a $(CN)_5Mn-NC-Fe(CN)_5$ cluster by an Ewald summation.[52] Since the main density difference between both states is at the Mn and Fe ions, ΔE_M can be approximated as

$$\Delta E_M = \frac{1}{2}\Delta Q(Fe)\{V^{LT}(Fe) - V^{HT}(Fe)\} +$$
$$\frac{1}{2}\Delta Q(Mn)\{V^{LT}(Mn) - V^{HT}(Mn)\} \quad (2)$$

where $\Delta Q(Fe)$ and $\Delta Q(Mn)$ are the charge population differences between the two electronic configurations for the iron and the manganese ions, respectively, and the Madelung potentials are evaluated at the position of their nuclei.

Table 4 records the Madelung potentials in the Fe and Mn ions for the HT and LT electronic configurations for two different models, called 1 and 2. The first model considers the charges of the transition-metal ions to be equal to their valencies, e.g., the charge of Mn^{2+} is +2, and the charges of N, C, and Rb are −1, 0, and +1, respectively, while the second, more realistic, model assigns the atomic charges for the LT and HT electronic configurations as derived from the periodic DFT calculations of the equilibrium structures and listed in Table 3.

The latter values show that even if one electron is transferred from the Fe ion to the Mn ion, the changes in charge population,

$\Delta Q(\text{Fe})$ and $\Delta Q(\text{Mn})$, are only around one-quarter of an electron, due to a compensating charge redistribution of the closed electronic shells. This implies not only lower values for $\Delta Q(\text{Fe})$ and $\Delta Q(\text{Mn})$ in model 2 with respect to model 1, but also more similar Madelung potentials for the LT and HT phases. Indeed, while a ΔE_M value of 4.4 eV obtained with the charge distribution of model 1 would invalidate the use of the periodic hybrid DFT method for computing the photoactivation energy, the mentioned charge redistribution produces a ΔE_M value of only 0.15 eV. Even this latter estimation of ΔE_M is rather crude since we considered the charge change between the ground and the Franck−Condon states to be concentrated at the Fe and Mn nuclei, just where the Madelung potentials show local maxima, and therefore, also the difference between the V_M^{LT} and V_M^{HT} Madelung potentials will be local maxima at those points. A more accurate calculation of ΔE_M by computing the integral in eq 1 would give an even lower value for ΔE_M. Therefore, the similar charge distribution in the LT and HT electronic states, despite the electron transfer between the transition metals, produces a low value of ΔE_M, allowing the qualitative determination of the photoactivation energy from periodic DFT calculations.

Finally, it is interesting to remark that this computational method has proved to be suitable for predicting the existence of a photoinduced phase transition in PBAs. However, to have a photomagnetic effect related to the photoinduced phase transition, the magnetic behavior of the two phases involved in the phase transition must be different. The study of the fulfillment of this last condition was beyond the scope of this work.

Conclusions

In this work, a periodic DFT method with the hybrid B3LYP exchange-correlation functional was used for studying the electron transfer that can be induced thermally or by irradiation in the RbMn[Fe(CN)₆] PBA. The method was able to correctly describe the unit cell parameters and the internal coordinates of the LT and HT phases, as well as their enthalpy difference. This and the correct description of the HT phase as a metastable phase, by computing a potential energy surface of both phases, support the suitability of the method for future prediction of PBAs as candidates for showing photomagnetic properties. Moreover, despite the periodic nature of the method and the local nature of the photoinduced charge transfer process, the periodic DFT method has also proved to be adequate for computing the photoactivation energy, although in this case it must be checked that the Franck−Condon state is a ground state for a particular spin value and that the charge distribution difference between the ground and photoexcited electronic configurations is not large. Finally, the direct application of this method to the study of compounds containing defects is not affordable due to the large increase in the size of the periodic model. However, computation of the PES of the pure system in combination with ab initio embedded cluster calculations of the electron affinity of the $[M(CN)_6]^{3-}$ complexes with no, one, or more cyano groups substituted by water molecules should allow the extension of the method to PBAs containing defects.

References and Notes

(1) Sato, O. J. *Photochem. Photobiol., C* **2004**, *5*, 203.
(2) Decurtins, S.; Gütlich, P.; Kohler, C. P.; Spiering, H.; Hauser, A. *Chem. Phys. Lett.* **1984**, *105*, 1.
(3) Decurtins, S.; Gütlich, P.; Kohler, C. P.; Spiering, H. *Chem. Commun.* **1985**, 430.
(4) Hauser, A. *J. Chem. Phys.* **1991**, *94*, 2741.
(5) Hauser, A. In *Spin Crossover in Transition Metal Compounds II*; Gütlich, P., Goodwin, H. A., Eds.; Topics in Current Chemistry 234; Springer: Berlin, 2004; p 155.
(6) Hayami, S.; Gu, Z. Z.; Shiro, M.; Einaga, Y.; Fujishima, A.; Sato, O. *J. Am. Chem. Soc.* **2000**, *122*, 7126.
(7) Juhasz, G.; Hayami, S.; Sato, O.; Maeda, Y. *Chem. Phys. Lett.* **2002**, *364*, 164.
(8) Hayami, S.; Hashiguchi, K.; Inoue, K.; Maeda, Y. *J. Nucl. Radiochem. Sci.* **2004**, *5*, N1.
(9) Boillot, M.-L.; Roux, C.; Audiere, J.-P.; Dausse, A.; Zarembowitch, J. *Inorg. Chem.* **1996**, *35*, 3975.
(10) Boillot, M.-L.; Chantraine, S.; Zarembowitch, J.; Lallemand, J.-Y.; Prunet, J. *New J. Chem.* **1999**, 179.
(11) Boillot, M.-L.; Zarembowitch, J.; Sour, A. In *Spin Crossover in Transition Metal Compounds II*; Gütlich, P., Goodwin, H. A., Eds.; Topics in Current Chemistry 234; Springer: Berlin, 2004; p 261.
(12) Roux, C.; Zarembowitch, J.; Gallois, B.; Granier, T.; Claude, R. *Inorg. Chem.* **1994**, *33*, 2273.
(13) Sour, A.; Boillot, M.-L.; Riviere, E.; Lesot, P. *Eur. J. Inorg. Chem.* **1999**, 2117.
(14) Carbonera, C.; Dei, A.; Letard, J.-F.; Sangregorio, C.; Sorace, L. *Angew. Chem., Int. Ed.* **2004**, *43*, 3136.
(15) Carbonera, C.; Dei, A.; Sangregorio, C.; Sorace, L. *Chem. Phys. Lett.* **2004**, *396*, 198.
(16) Dei, A.; Gatteschi, D.; Sangregorio, C.; Sorace, L. *Acc. Chem. Res.* **2004**, *37*, 827.
(17) Hendrickson, D. N.; Pierpont, C. G. In *Spin Crossover in Transition Metal Compounds II*; Gutlich, P., Goodwin, H. A., Eds.; Topics in Current Chemistry 234; Springer: Berlin, 2004; p 63.
(18) Neuwahl, F. V. R.; Righini, R.; Dei, A. *Chem. Phys. Lett.* **2002**, *352*, 408.
(19) Sato, O.; Hayami, S.; Gu, Z. Z.; Seki, K.; Nakajima, R.; Fujishima, A. *Chem. Lett.* **2001**, 874.
(20) Caneschi, A.; Dei, A. *Angew. Chem., Int. Ed.* **1998**, *37*, 3005.
(21) Sato, O.; Iyoda, T.; Fujishima, A.; Hashimoto, K. *Science* **1996**, *272*, 704.
(22) Verdaguer, M. *Science* **1996**, *272*, 698.
(23) Tokoro, H.; Ohkoshi, S.-I.; Hashimoto, K. *Appl. Phys. Lett.* **2003**, *82*, 1245.
(24) Ohkoshi, S.-I.; Hashimoto, K. *J. Am. Chem. Soc.* **1999**, *121*, 10591.
(25) Carducci, M. D.; Pressprich, M. R.; Coppens, P. *J. Am. Chem. Soc.* **1997**, *119*, 2669.
(26) Coppens, P.; Fomitchev, D. V.; Carducci, M. D.; Culp, K. *J. Chem. Soc., Dalton Trans.* **1998**, 865.
(27) Gu, Z. Z.; Sato, O.; Iyoda, T.; Hashimoto, K.; Fujishima, A. *J. Phys. Chem.* **1996**, *100*, 18289.
(28) Schaniel, D.; Schefer, J.; Imlau, M.; Woike, Th. *Phys. Rev. B* **2003**, *68*, 104108.
(29) Ohkoshi, S.-I.; Machida, N.; Zhong, Z. J.; Hashimoto, K. *Synth. Met.* **2001**, *122*, 523.
(30) Rombaut, G.; Verelst, M.; Golhen, S.; Ouahab, L.; Mathoniere, C.; Kahn, O. *Inorg. Chem.* **2001**, *40*, 1151.
(31) Mathoniere, C.; Podgajny, R.; Guionneau, P.; Labrugere, C.; Sieklucka, B. *Chem. Mater.* **2005**, *17*, 442.
(32) Arimoto, Y.; Ohkoshi, S.-I.; Zhong, Z. J.; Seino, H.; Mizobe, Y.; Hashimoto, K. *J. Am. Chem. Soc.* **2003**, *125*, 9240.
(33) Becke, A. D. *J. Chem. Phys.* **1993**, *98*, 5648–5652.
(34) Bredow, T.; Gerson, A. R. *Phys. Rev. B* **2000**, *61*, 5194.
(35) Muscat, J.; Wander, A.; Harrison, N. M. *Chem. Phys. Lett.* **2001**, *342*, 397.
(36) Ohkoshi, S.-I.; Tokoro, H.; Utsunomiya, M.; Mizuno, M.; Abe, M.; Hashimoto, K. *J. Phys. Chem. B* **2002**, *106*, 2423.

Luzon et al.

(37) Moritomo, Y.; Kato, K.; Kuriki, A.; Takata, M.; Sakata, M.; Tokoro, H.; Ohkoshi, S.-I.; Hashimoto, K. *J. Phys. Soc. Jpn.* **2002**, *71*, 2078.

(38) Osawa, H.; Iwazumi, T.; Tokoro, H.; Ohkoshi, S.-I.; Hashimoto, K.; Shoji, H.; Hirai, E.; Nakamura, T.; Nanao, S.; Isozumi, Y. *Solid State Commun.* **2003**, *125*, 237.

(39) Moritomo, Y.; Kuriki, A.; Ohoyama, K.; Tokoro, H.; Ohkoshi, S.-I.; Hashimoto, K.; Hamada, N. *J. Phys. Soc. Jpn.* **2003**, *72*, 456.

(40) Vertelman, E. J. M.; Maccallini, E.; Gournis, D.; Rudolf, P.; Bakas, T.; Luzon, J.; Broer, R.; Pugzlys, A.; Lummen, T. T. A.; van Loosdrecht, P. H. M.; van Koningsbruggen, P. J *Chem. Mater.* **2006**, *18*, 1951.

(41) Tougaard, S. *Surf. Interface Anal.* **1997**, *25*, 137.

(42) Saunders, V. R.; Dovesi, R.; Roetti, C.; Orlando, R.; Zicovich-Wilson, C. M.; Harrison, N. M.; Doll, K.; Civalleri, B.; Bush, I. J.; D'Arco, P.; Llunell, M. *Crystal03 User's Manual*; Universita di Torino: Torino, Italy, 2003.

(43) Moreira, I. de P. R.; Dovesi R. *Int. J. Quantum Chem.* **2004**, *99*, 805.

(44) www.crystal.unito.it/Basis_Sets/ptable.html.

(45) Kato, K.; Moritomo, Y.; Takata, M.; Sakata, M.; Umekawa, M.; Hamada, N.; Ohkoshi, S.-I.; Tokoro, H.; Hashimoto, K. *Phys. Rev. Lett.* **2003**, *91*, 25502.

(46) Cobo, S.; Fernandez, R.; Salmon, L.; Molnar, G.; Bousseksou, A. *Eur. J. Inorg. Chem.* **2007**, 1549.

(47) Tokoro, H.; Ohkoshi, S.-I.; Matsuda, T.; Hashimoto, K. *Inorg. Chem.* **2004**, *43*, 5231.

(48) Zwijnenburg, M. A.; Cora, F.; Bell, R. G. *J. Phys. Chem. B* **2007**, *111*, 6156.

(49) Yokoyama, T.; Tokoro, H.; Ohkoshi, S.-I.; Hashimoto, K.; Okamoto, K.; Ohta, T. *Phys. Rev. B* **2002**, *66*, 184111–1.

(50) Moritomo, Y.; Hanawa, M.; Ohishi, Y.; Kato, K.; Takata, M.; Kuriki, A.; Nishibori, E.; Sakata, M. *Phys. Rev. B* **2003**, *68*, 144106.

(51) Moritomo, Y.; Kato, K.; Kuriki, A.; Takata, M.; Sakata, M.; Tokoro, H.; Ohkoshi, S.-I.; Hashimoto, K. *J. Phys. Soc. Jpn.* **2003**, *72*, 2698.

(52) Ewald, P. P. *Ann. Phys.* **1921**, *64*, 253.